SCIENCE CHINA
Information Sciences

• RESEARCH PAPER •

August 2017, Vol. 60 082304:1–082304:13
doi: 10.1007/s11432-016-9004-4

3D non-stationary wideband circular tunnel channel models for high-speed train wireless communication systems

Yu LIU[1], Cheng-Xiang WANG[1,2*], Carlos LOPEZ[2] & Xiaohu GE[3]

[1]*Shandong Provincial Key Lab of Wireless Communication Technologies, Shandong University, Jinan* 250100*, China;*
[2]*Institute of Sensors, Signals and Systems, School of Engineering & Physical Sciences, Heriot-Watt University, Edinburgh* EH14 4AS*, U.K.;*
[3]*Department of Electronics and Information Engineering, Huazhong University of Science and Technology, Wuhan* 430074*, China*

Received October 30, 2016; accepted November 30, 2016; published online March 13, 2017

Abstract This paper proposes three-dimensional (3D) non-stationary wideband circular geometry-based stochastic models (GBSMs) for high-speed train (HST) tunnel scenarios. Considering single-bounced (SB) and multiple-bounced (MB) components from the tunnel's internal surfaces, a theoretical channel model is first established. Then, the corresponding simulation model is developed using the method of equal volume (MEV) to calculate discrete angular parameters. Based on the proposed 3D GBSMs, important time-variant statistical properties are investigated, such as the temporal autocorrelation function (ACF), spatial cross-correlation function (CCF), and space-Doppler (SD) power spectrum density (PSD). Results indicate that all statistical properties of the simulation model, verified by simulation results, can match well those of the theoretical model. The statistical properties of the proposed 3D GBSMs are further validated by relevant measurement data, demonstrating the flexibility and utility of our proposed tunnel GBSMs.

Keywords non-stationary, statistical properties, tunnel channel model, GBSM, channel measurement

Citation Liu Y, Wang C-X, Lopez C, et al. 3D non-stationary wideband circular tunnel channel models for high-speed train wireless communication systems. Sci China Inf Sci, 2017, 60(8): 082304, doi: 10.1007/s11432-016-9004-4

1 Introduction

With the increasing demands of high-speed train (HST) users, numerous communication data need to be transmitted through wireless channels with the fifth generation (5G) communication networks [1]. Hence, high-capacity and reliable HST communication networks are required. HSTs may encounter more than 12 scenarios when traveling [2], such as open space, cutting, viaduct, and tunnels. Due to the confined space of tunnel, waveguide effects, and poor smoothness of interior walls, propagation characteristics of signals inside tunnels are quite different from those in other HST scenarios. Radio signals inside tunnels will suffer more reflections, diffractions, and scattering.

Some existing HST channel models, e.g., in [3], cannot be applied to describe the propagation conditions of tunnel channels accurately. To better develop future tunnel communication systems, it does require

* Corresponding author (email: cheng-xiang.wang@hw.ac.uk)

a comprehensive understanding of statistical properties for tunnel channels and accurate HST tunnel channel models. Variety of tunnel channel models have been developed based on different modeling methods [4], such as geometrical optics (GO) [5,6], the modal theory [7], and finite-state Markov models (FSMMs) [8,9]. A GO approach in [10] can be applied to predict the path loss (PL) and signal propagation delay at any location. However, it needs a detailed description of tunnel environment [11]. Considering the tunnel geometry and electrical conductivity of tunnel walls, the signals propagation inside tunnel can be modeled as same with those in a waveguide. A waveguide tunnel channel model has been introduced in [12]. Since rapid attenuation of high order modes, this kind of model can characterize only the lowest-order mode signal propagating in far region, and ignore the multi-mode case in near region [13]. Therefore, a waveguide model should be combined with another model, which can be used to model the multi-mode cases, to model a completed HST tunnel channel. In [14], a multi-mode tunnel channel model that combined the waveguide model and GO model was developed. Research work in [8] has proposed an FSMM for tunnel channels by gathering the real measurements. In this model, tunnel can be divided into intervals, and FSMM can be applied in each distance interval. Most of the aforementioned work are focused on large-scale fading [15]. Few studies have focused on the small-scale fading channel modeling. Based on the model proposed in [14], a time-dependent multi-mode channel model for HST tunnels was further investigated [16], and some small-scale fading characteristics were also presented. In [17], a three-dimensional (3D) vehicle-to-vehicle (V2V) wide-sense stationary (WSS) geometry-based stochastic model (GBSM) for road tunnels was proposed, and some small-scale fading characteristics has been analyzed. However, HST channel measurements have indicated that the underlying channels are mostly non-stationary. To the best of the authors' knowledge, non-stationary GBSMs for HST tunnels have not been studied. The GBSMs, such as 2D one-ring, two-ring, elliptical, and 3D ellipse cylinder models [18], constitute an important part of channel models, but can not be utilized to describe the propagation characteristics of tunnel channels. In this paper, we aim to develop 3D non-stationary GBSMs for HST circular tunnel scenarios based on the real tunnel shape, then assumed the clusters are located on the internal surface of tunnel, and further investigate some time-variant statistical properties. The proposed models will be verified by measurement channel characteristics.

The remainder of this paper is structured as follows. In Section 2, the 3D non-stationary wideband theoretical GBSM for circular tunnel channels is presented. Section 3 describes the simulation GBSM. Results and analysis are given in Section 4. Finally, conclusion is drawn in Section 5.

2 A non-stationary theoretical GBSM for circular tunnel channels

2.1 Description of the non-stationary wideband theoretical circular tunnel channel model

In this section, a typical HST tunnel wireless network architecture including distributed antenna system (DAS), multiple-input multiple-output (MIMO) technology, and mobile relay station (MRS) is considered [19–22]. The DAS can provide better coverage inside tunnel, the MRS can be applied to improve the quality of received signals, and the MIMO technology can be used to obtain higher capacity. The combination of these technologies can provide higher reliability and availability for the tunnel wireless communication systems. Based on this architecture, channel models for the most classical circular tunnel channels are developed, as shown in Figure 1.

The cross section of this tunnel is approximately circular-shape. The radius of tunnel is set as R, the transmitter (Tx) is placed along side wall, and the receiver (Rx) is placed at the center of the tunnel cross section. Here, we abstract the circular-shape tunnel as a hollow cylinder [23], with the origin located at the beginning of the tunnel. A 3D cylinder-shape GBSM for circular tunnel scenarios is presented in Figure 2, which can be used to describe the scattering environments inside tunnel. It is assumed that there are I_{cluster} clusters randomly distributed on the internal surfaces of tunnel walls [24]. The position of cluster in single-bounced (SB) case can be determined by the azimuth angle of arrival (AAoA) and elevation angle of arrival (EAoA), and the positions of clusters in multiple-bounced (MB) case can be acquired by the AAoA and EAoA at Rx, and the azimuth angle of departure (AAoD) and elevation angle

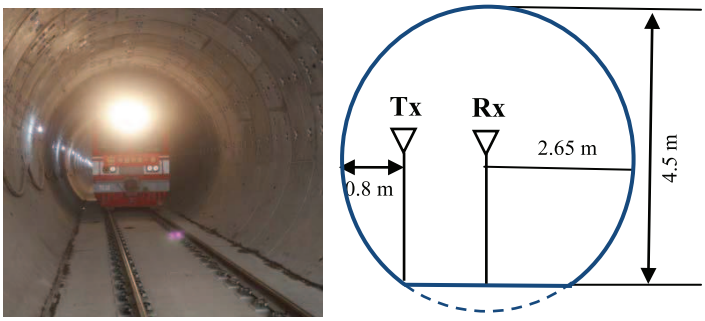

Figure 1 (Color online) HST circular tunnel wireless communication system.

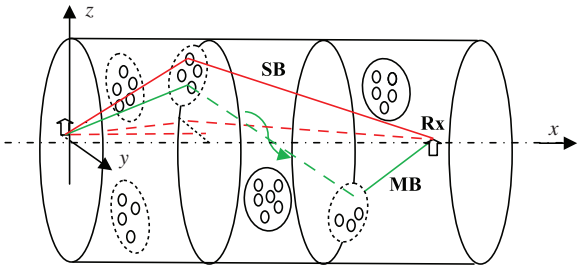

Figure 2 (Color online) 3D cylinder-shape GBSM for circular tunnel scenarios.

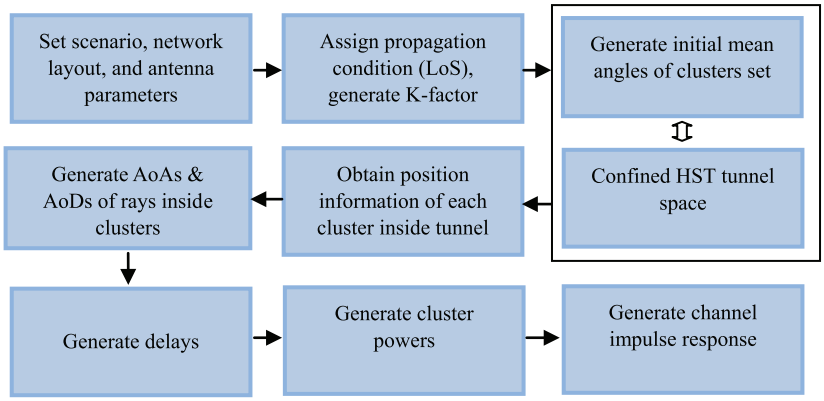

Figure 3 (Color online) The non-stationary circular tunnel channel coefficients generation procedure.

of departure (EAoD) at Tx. Each cluster scatters an infinite number of rays. Based on the aforementioned geometric description, a flowchart of channel coefficients generation procedure is illustrated in Figure 3.

The complex channel impulse response $h_{pq}(t,\tau)$ between the pth ($p=1,2,\ldots,U_{\mathrm{T}}$) Tx and qth ($q=1,2,\ldots,U_{\mathrm{R}}$) Rx is the superposition of line-of-sight (LoS), SB, and MB components, which can be expressed as

$$h_{pq}(t,\tau)=\left(h_{pq,i}^{\mathrm{LoS}}(t)\cdot\delta(i-1)+\sum_{i=1}^{I'_{\mathrm{cluster}}}h_{pq,i}^{\mathrm{SB}}(t)\right)\cdot\delta(\tau-\tau_i^{\mathrm{SB}}(t))+\sum_{l=1}^{I''_{\mathrm{cluster}}}h_{pq,l}^{\mathrm{MB}}(t)\cdot\delta(\tau-\tau_l^{\mathrm{MB}}(t)).\tag{1}$$

For the LoS component, the channel gain can be presented as

$$h_{pq,1}^{\mathrm{LoS}}(t)=\sqrt{\frac{K_{pq}}{K_{pq}+1}}\mathrm{e}^{-\mathrm{j}\frac{2\pi}{\lambda}\cdot D_{pq}(t)}$$

$$\times \mathrm{e}^{\mathrm{j}2\pi f_{\mathrm{Rmax}} t\cdot\cos(\alpha_{\mathrm{R}}^{\mathrm{LoS}}(t)-\gamma_{\mathrm{R}})\cdot\cos\beta_{\mathrm{R}}^{\mathrm{LoS}}(t)}. \tag{2}$$

In addition, for the SB component, we can get

$$h_{pq,i}^{\mathrm{SB}}(t)=\sqrt{\frac{P_i}{K_{pq}+1}}\lim_{N_i\to\infty}\sum_{n_i=1}^{N_i}\frac{1}{\sqrt{N_i}}\mathrm{e}^{\mathrm{j}(\varphi_{n_i}-\frac{2\pi}{\lambda}\cdot D_{pq}^{in_i}(t))} \times \mathrm{e}^{\mathrm{j}2\pi f_{\mathrm{Rmax}} t\cdot\cos(\alpha_{\mathrm{R}}^{in_i}(t)-\gamma_{\mathrm{R}})\cdot\cos\beta_{\mathrm{R}}^{in_i}(t)}, \tag{3}$$

here, the distance $D_{pq}^{in_i}(t)$ can be computed by $D_{p\mathrm{T}}^{in_i}(t)$ and $D_{q\mathrm{R}}^{in_i}(t)$, which can be expressed as

$$D_{pq}^{in_i}(t)=D_{p\mathrm{T}}^{in_i}(t)+D_{q\mathrm{R}}^{in_i}(t), \tag{4}$$

$$D_{p\mathrm{T}}^{in_i}(t)=\sqrt{(x_{p\mathrm{T}}-x_{in_i})^2+(y_{p\mathrm{T}}-y_{in_i})^2+(z_{p\mathrm{T}}-z_{in_i})^2}, \tag{5}$$

$$D_{q\mathrm{R}}^{in_i}(t)=\sqrt{(x_{q\mathrm{R}}-x_{in_i})^2+(y_{q\mathrm{R}}-y_{in_i})^2+(z_{q\mathrm{R}}-z_{in_i})^2}. \tag{6}$$

In (5), the coordinates of the pth antenna element of Tx $(x_{p\mathrm{T}}, y_{p\mathrm{T}}, z_{p\mathrm{T}})$ are derived as

$$x_{p\mathrm{T}}=x_{\mathrm{T}}+k_p\cdot\Delta_{\mathrm{T}}\cdot\cos\phi_{\mathrm{T}}\cdot\cos\varphi_{\mathrm{T}}, \tag{7}$$

$$y_{p\mathrm{T}}=y_{\mathrm{T}}+k_p\cdot\Delta_{\mathrm{T}}\cdot\cos\phi_{\mathrm{T}}\cdot\sin\varphi_{\mathrm{T}}, \tag{8}$$

$$z_{p\mathrm{T}}=z_{\mathrm{T}}+k_p\cdot\Delta_{\mathrm{T}}\cdot\sin\phi_{\mathrm{T}}. \tag{9}$$

Then, the coordinates of the qth antenna element of Rx in (6) are

$$x_{q\mathrm{R}}=x_{\mathrm{R}}+k_q\cdot\Delta_{\mathrm{R}}\cdot\cos\phi_{\mathrm{R}}\cdot\cos\varphi_{\mathrm{R}}, \tag{10}$$

$$y_{q\mathrm{R}}=y_{\mathrm{R}}+k_q\cdot\Delta_{\mathrm{R}}\cdot\cos\phi_{\mathrm{R}}\cdot\sin\varphi_{\mathrm{R}}, \tag{11}$$

$$z_{q\mathrm{R}}=z_{\mathrm{R}}+k_q\cdot\Delta_{\mathrm{R}}\cdot\sin\phi_{\mathrm{R}}. \tag{12}$$

Moreover, the coordinates $(x_{in_i}(t), y_{in_i}(t), z_{in_i}(t))$ of n_ith ray of ith cluster are denoted by

$$x_{in_i}(t)=x_{\mathrm{R}}-v_{\mathrm{R}}t-\mathrm{D}_{\mathrm{R}}^{in_i}(t)\cdot\cos\beta_{\mathrm{R}}^{in_i}(t)\cdot\cos\alpha_{\mathrm{R}}^{in_i}(t), \tag{13}$$

$$y_{in_i}(t)=y_{\mathrm{R}}-\mathrm{D}_{\mathrm{R}}^{in_i}(t)\cdot\cos\beta_{\mathrm{R}}^{in_i}(t)\cdot\sin\alpha_{\mathrm{R}}^{in_i}(t), \tag{14}$$

$$z_{in_i}(t)=z_{\mathrm{R}}-\mathrm{D}_{\mathrm{R}}^{in_i}(t)\cdot\sin\beta_{\mathrm{R}}^{in_i}(t). \tag{15}$$

It is worth mentioning that, the time-variant $\alpha_{\mathrm{R}}^{in_i}(t)$, $\beta_{\mathrm{R}}^{in_i}(t)$ can be obtained from the mean AAoAs $\alpha_{\mathrm{R}}^{i}(t)$ and EAoAs $\beta_{\mathrm{R}}^{i}(t)$ of ith cluster, which are derived as

$$\alpha_{\mathrm{R}}^{i}(t)=\arctan\frac{D_{\mathrm{R}}^{i}(t_0)\cos\beta_{\mathrm{R}}^{i}(t_0)\sin\alpha_{\mathrm{R}}^{i}(t_0)}{D_{\mathrm{R}}^{i}(t_0)\cos\beta_{\mathrm{R}}^{i}(t_0)\cos\alpha_{\mathrm{R}}^{i}(t_0)-v_{c\mathrm{R}}t-v_{\mathrm{R}}t}, \tag{16}$$

and

$$\beta_{\mathrm{R}}^{i}(t)=\arctan\frac{D_{\mathrm{R}}^{i}(t_0)\sin\beta_{\mathrm{R}}^{i}(t_0)}{\sqrt{(D_{\mathrm{R}}^{i}(t_0)\cos\beta_{\mathrm{R}}^{i}(t_0)\sin\alpha_{\mathrm{R}}^{i}(t_0))^2+(D_{\mathrm{R}}^{i}(t_0)\cos\beta_{\mathrm{R}}^{i}(t_0)\cos\alpha_{\mathrm{R}}^{i}(t_0)-v_{c\mathrm{R}}t-v_{\mathrm{R}}t)^2}}. \tag{17}$$

In the same way, the channel gain for the MB components can be expressed as

$$h_{pq,l}^{\mathrm{MB}}(t)=\sqrt{\frac{P_l}{K_{pq}+1}}\lim_{N_l\to\infty}\sum_{n_l=1}^{N_l}\frac{1}{\sqrt{N_l}}\mathrm{e}^{\mathrm{j}(\varphi_{n_l}-\frac{2\pi}{\lambda}\cdot D_{pq}^{ln_l}(t))} \times \mathrm{e}^{\mathrm{j}2\pi f_{\mathrm{Rmax}} t\cdot\cos(\alpha_{\mathrm{R}}^{ln_l}(t)-\gamma_{\mathrm{R}})\cdot\cos\beta_{\mathrm{R}}^{ln_l}(t)}, \tag{18}$$

where

$$D_{pq}^{ln_l}(t) = D_{p\mathrm{T}}^{ln_l}(t) + D_{q\mathrm{R}}^{ln_l}(t) + \widetilde{\tau}_{pq,n_l}(t) \cdot c, \tag{19}$$

$$D_{p\mathrm{T}}^{ln_l}(t) = \sqrt{\left(x_{p\mathrm{T}} - x_{ln_l}^{\mathrm{T}}\right)^2 + \left(y_{p\mathrm{T}} - y_{ln_l}^{\mathrm{T}}\right)^2 + \left(z_{p\mathrm{T}} - z_{ln_l}^{\mathrm{T}}\right)^2}, \tag{20}$$

$$D_{q\mathrm{R}}^{ln_l}(t) = \sqrt{\left(x_{q\mathrm{R}} - x_{ln_l}^{\mathrm{R}}\right)^2 + \left(y_{q\mathrm{R}} - y_{ln_l}^{\mathrm{R}}\right)^2 + \left(z_{q\mathrm{R}} - z_{ln_l}^{\mathrm{R}}\right)^2}. \tag{21}$$

Here, the coordinates $(x_{ln_l}^{\mathrm{T}}(t), y_{ln_l}^{\mathrm{T}}(t), z_{ln_l}^{\mathrm{T}}(t))$ of n_lth ray of lth cluster at Tx are given by

$$x_{ln_l}^{\mathrm{T}}(t) = x_{\mathrm{T}} + \mathrm{D}_{\mathrm{T}}^{ln_l}(t) \cdot \cos\beta_{\mathrm{T}}^{ln_l}(t) \cdot \cos\alpha_{\mathrm{T}}^{ln_l}(t), \tag{22}$$

$$y_{ln_l}^{\mathrm{T}}(t) = y_{\mathrm{T}} + \mathrm{D}_{\mathrm{T}}^{ln_l}(t) \cdot \cos\beta_{\mathrm{T}}^{ln_l}(t) \cdot \sin\alpha_{\mathrm{T}}^{ln_l}(t), \tag{23}$$

$$z_{ln_l}^{\mathrm{T}}(t) = z_{\mathrm{T}} + \mathrm{D}_{\mathrm{T}}^{ln_l}(t) \cdot \sin\beta_{\mathrm{T}}^{ln_l}(t). \tag{24}$$

Then, the coordinates $(x_{ln_l}^{\mathrm{R}}(t), y_{ln_l}^{\mathrm{R}}(t), z_{ln_l}^{\mathrm{R}}(t))$ of n_lth ray of lth cluster at Rx can be expressed as

$$x_{ln_l}^{\mathrm{R}}(t) = x_{\mathrm{R}} - v_{\mathrm{R}}t - \mathrm{D}_{\mathrm{R}}^{ln_l}(t) \cdot \cos\beta_{\mathrm{R}}^{ln_l}(t) \cdot \cos\alpha_{\mathrm{R}}^{ln_l}(t), \tag{25}$$

$$y_{ln_l}^{\mathrm{R}}(t) = y_{\mathrm{R}} - \mathrm{D}_{\mathrm{R}}^{ln_l}(t) \cdot \cos\beta_{\mathrm{R}}^{ln_l}(t) \cdot \sin\alpha_{\mathrm{R}}^{ln_l}(t), \tag{26}$$

$$z_{ln_l}^{\mathrm{R}}(t) = z_{\mathrm{R}} - \mathrm{D}_{\mathrm{R}}^{ln_l}(t) \cdot \sin\beta_{\mathrm{R}}^{ln_l}(t). \tag{27}$$

The corresponding distance $D_{\mathrm{T}}^{ln_l}(t)$ can be expressed as

$$D_{\mathrm{T}}^{ln_l}(t) = \frac{-2 \cdot (\cos\beta_{\mathrm{T}}^{ln_l}(t) \cdot \sin\alpha_{\mathrm{T}}^{ln_l}(t) \cdot y_{\mathrm{T}} + \sin\beta_{\mathrm{T}}^{ln_l}(t) \cdot z_{\mathrm{T}}) + \sqrt{L(t)}}{2(\cos^2\beta_{\mathrm{T}}^{ln_l}(t) \cdot \sin^2\alpha_{\mathrm{T}}^{ln_l}(t) + \sin^2\beta_{\mathrm{T}}^{ln_l}(t))}, \tag{28}$$

here, we have

$$\begin{aligned} L(t) = {} & 4(\cos\beta_{\mathrm{T}}^{ln_l}(t) \cdot \sin\alpha_{\mathrm{T}}^{ln_l}(t) \cdot y_{\mathrm{T}} + \sin\beta_{\mathrm{T}}^{ln_l}(t) \cdot z_{\mathrm{T}})^2 \\ & - 4(\cos^2\beta_{\mathrm{T}}^{ln_l}(t) \cdot \sin^2\alpha_{\mathrm{T}}^{ln_l}(t) + \sin^2\beta_{\mathrm{T}}^{ln_l}(t))(y_{\mathrm{T}}^2 + z_{\mathrm{T}}^2 - R^2). \end{aligned} \tag{29}$$

While the distance $D_{\mathrm{R}}^{ln_l}(t)$ can be presented as

$$D_{\mathrm{R}}^{ln_l}(t) = \frac{R}{\sqrt{1 - \cos^2\beta_{\mathrm{R}}^{ln_l}(t)\cos^2\alpha_{\mathrm{R}}^{ln_l}(t)}}. \tag{30}$$

In (7)–(12), $k_p = (U_{\mathrm{T}} - 2p + 1)/2$, $k_q = (U_{\mathrm{R}} - 2q + 1)/2$. The symbol K_{pq} designates the LoS Ricean factor, and c represents the speed of light. The phases φ_{n_i}, φ_{n_l} are independent and identically distributed (i.i.d.) random variables with uniform distributions. The delay $\tilde{\tau}_{pq,n_l}(t)$ of the virtual link between two clusters can be generated randomly with exponential delay distribution or uniform distribution initially [25]. For each cluster, the mean power P_i of ith cluster in SB, and P_l of lth twin-cluster in MB, are both generated as WINNER II channel model as [25]

$$\mathrm{P}_{i/l} = \mathrm{e}^{\frac{(1-r_\tau)\tau_{i/l}}{r_\tau\sigma_\tau}} \times 10^{\frac{Z_{i/l}}{10}}, \tag{31}$$

where r_τ denotes the delay scaling parameter, σ_τ is randomly generated delay spread, and $Z_{i/l}$ is shadowing term of each cluster, which follows the Gaussian distribution.

By using the initial AAoD $\alpha_{\mathrm{T}}^l(t_0)$ and EAoD $\beta_{\mathrm{T}}^l(t_0)$ of lth twin-cluster, the time-variant mean AAoD $\alpha_{\mathrm{T}}^l(t)$ and EAoD $\beta_{\mathrm{T}}^l(t)$ of lth twin-cluster can be expressed as

$$\alpha_{\mathrm{T}}^l(t) = \arctan\frac{D_{\mathrm{T}}^l(t_0)\cos\beta_{\mathrm{T}}^l(t_0)\sin\alpha_{\mathrm{T}}^l(t_0)}{D_{\mathrm{T}}^l(t_0)\cos\beta_{\mathrm{T}}^l(t_0)\cos\alpha_{\mathrm{T}}^l(t_0) - v_{c\mathrm{T}}t}, \tag{32}$$

$$\beta_{\mathrm{T}}^l(t) = \arctan\frac{D_{\mathrm{T}}^l(t_0)\sin\beta_{\mathrm{T}}^l(t_0)}{\sqrt{(D_{\mathrm{T}}^l(t_0)\cos\beta_{\mathrm{T}}^l(t_0)\sin\alpha_{\mathrm{T}}^l(t_0))^2 + (D_{\mathrm{T}}^l(t_0)\cos\beta_{\mathrm{T}}^l(t_0)\cos\alpha_{\mathrm{T}}^l(t_0) - v_{c\mathrm{T}}t)^2}}. \tag{33}$$

Meanwhile, the time-variant mean AAoA, EAoA at Rx in MB can be obtained by similar method in (16), (17) in SB case. The mentioned parameters above are defined in Table 1.

Table 1 Definition of model parameter

Parameter	Definition
$D_{pq}(t)$	Distance of LoS between the Tx and Rx
$D_{pq}^{in_i}(t)$	Distance of n_i ray of ith cluster between Tx and Rx in SB
$D_{p\mathrm{T}}^{in_i}(t)$	Distance of n_i ray of ith cluster between Tx and ith cluster in SB
$D_{q\mathrm{R}}^{in_i}(t)$	Distance of n_i ray of ith cluster between ith cluster and Rx in SB
$\alpha_{\mathrm{T}}^{in_i}(t), \beta_{\mathrm{T}}^{in_i}(t)$	AAoD and EAoD of n_ith ray of ith cluster in SB
$\alpha_{\mathrm{R}}^{in_i}(t), \beta_{\mathrm{R}}^{in_i}(t)$	AAoA and EAoA of n_ith ray of ith cluster in SB
$v_{c\mathrm{T}}, v_{c\mathrm{R}}$	Velocities of clusters at Tx and Rx, respectively
$D_{pq}^{ln_l}(t)$	Distance of n_lth ray of lth cluster between Tx and Rx in MB
$D_{p\mathrm{T}}^{ln_l}(t)$	Distance of n_lth ray of lth cluster between Tx and lth cluster in MB
$D_{q\mathrm{R}}^{ln_l}(t)$	Distance of n_lth ray of lth cluster between lth cluster and Rx in MB
$\alpha_{\mathrm{T}}^{ln_l}(t), \beta_{\mathrm{T}}^{ln_l}(t)$	AAoD and EAoD of n_lth ray of lth cluster in MB
$\alpha_{\mathrm{R}}^{ln_l}(t), \beta_{\mathrm{R}}^{ln_l}(t)$	AAoA and EAoA of n_lth ray of lth cluster in MB
$\Delta_{\mathrm{R}}, \Delta_{\mathrm{T}}$	Antenna element spacings of Tx and Rx, respectively
v_{R}	Velocity of Rx in SB and MB
f_{Rmax}	Maximum Doppler shift of Rx
$\varphi_{\mathrm{T}}, \varphi_{\mathrm{R}}$	Azimuth angles of the Tx and Rx antenna array, respectively
$\phi_{\mathrm{T}}, \phi_{\mathrm{R}}$	Elevation angles of the Tx and Rx antenna array, respectively

2.2 Statistical properties in HST circular tunnel scenarios

2.2.1 *Time-variant space-time (ST) correlation function (CF)*

The time-variant ST CF can be derived as follows [18]:

$$R_h(t, \Delta x_{\mathrm{T}}, \Delta x_{\mathrm{R}}, \Delta t) = \mathrm{E}\left[h_{pq}(t) \cdot h_{p'q'}^{*}(t-\Delta t)\right]. \tag{34}$$

Here, we assumed the reflections from tunnel internal walls are independent of each other. Hence, the ST CF can be also expressed as

$$\begin{aligned} R_h(t, \Delta x_{\mathrm{T}}, \Delta x_{\mathrm{R}}, \Delta t) = {} & R_h^{\mathrm{LoS}}(t, \Delta x_{\mathrm{T}}, \Delta x_{\mathrm{R}}, \Delta t) + R_h^{\mathrm{SB}}(t, \Delta x_{\mathrm{T}}, \Delta x_{\mathrm{R}}, \Delta t) \\ & + R_h^{\mathrm{MB}}(t, \Delta x_{\mathrm{T}}, \Delta x_{\mathrm{R}}, \Delta t). \end{aligned} \tag{35}$$

The ST CF of the LoS, SB, and MB components can be expressed as follows:

(1) In the case of LoS component

$$\begin{aligned} R_h^{\mathrm{LoS}}(t, \Delta x_{\mathrm{T}}, \Delta x_{\mathrm{R}}, \Delta t) = {} & \frac{K_{pq}}{K_{pq}+1} \cdot \mathrm{e}^{\frac{\mathrm{j}2\pi}{\lambda} \cdot (D_{p'q'}(t-\Delta t) - D_{pq}(t))} \\ & \times \mathrm{e}^{\mathrm{j}2\pi f_{\mathrm{Rmax}} \cdot \Delta t \cdot \cos(\alpha_{\mathrm{R}}^{\mathrm{LoS}}(t-\Delta t) - \gamma_{\mathrm{R}}) \cdot \cos \beta_{\mathrm{R}}^{\mathrm{LoS}}(t-\Delta t)}. \end{aligned} \tag{36}$$

(2) In the case of SB component

$$\begin{aligned} R_h^{\mathrm{SB}}(t, \Delta x_{\mathrm{T}}, \Delta x_{\mathrm{R}}, \Delta t) = {} & \frac{P_i}{(K_{pq}+1)N_i} \int_{-\pi}^{\pi} \int_{-\pi/2}^{\pi/2} \mathrm{e}^{\frac{\mathrm{j}2\pi}{\lambda} \cdot (D_{p'q'}^{in_i}(t-\Delta t) - D_{pq}^{in_i}(t))} \\ & \times \mathrm{e}^{\mathrm{j}2\pi f_{\mathrm{Rmax}} \Delta t \cdot \cos(\alpha_{\mathrm{R}}^{in_i} - \gamma_{\mathrm{R}}) \cdot \cos \beta_{\mathrm{R}}^{in_i}} \cdot f(\alpha_{\mathrm{R}}^{in_i}, \beta_{\mathrm{R}}^{in_i}) \mathrm{d}(\alpha_{\mathrm{R}}^{in_i}, \beta_{\mathrm{R}}^{in_i}). \end{aligned} \tag{37}$$

(3) In the case of MB component

$$\begin{aligned} R_h^{\mathrm{MB}}(t, \Delta x_{\mathrm{T}}, \Delta x_{\mathrm{R}}, \Delta t) = {} & \frac{P_l}{(K_{pq}+1)N_l} \int_{-\pi}^{\pi} \int_{-\pi/2}^{\pi/2} \mathrm{e}^{\frac{\mathrm{j}2\pi}{\lambda} \cdot (D_{p'q'}^{ln_l}(t-\Delta t) - D_{pq}^{ln_l}(t))} \\ & \times \mathrm{e}^{\mathrm{j}2\pi f_{\mathrm{Rmax}} \Delta t \cos(\alpha_{\mathrm{R}}^{ln_l} - \gamma_{\mathrm{R}}) \cos \beta_{\mathrm{R}}^{ln_l}} \cdot f(\alpha_{\mathrm{R}}^{ln_l}, \beta_{\mathrm{R}}^{ln_l}) \mathrm{d}(\alpha_{\mathrm{R}}^{ln_l}, \beta_{\mathrm{R}}^{ln_l}). \end{aligned} \tag{38}$$

By imposing $\Delta t = 0$ in (35), the time-variant spatial cross-correlation function (CCF) can be expressed as

$$\rho_h(t, \Delta x_{\mathrm{T}}, \Delta x_{\mathrm{R}}) = R_h(t, \Delta x_{\mathrm{T}}, \Delta x_{\mathrm{R}}, 0). \tag{39}$$

On the other hand, by setting antenna elements spacings $\Delta x_{\mathrm{R}} = 0$ and $\Delta x_{\mathrm{T}} = 0$, the autocorrelation function (ACF) is obtained

$$r_h(t, \Delta t) = R_h(t, 0, 0, \Delta t). \tag{40}$$

2.2.2 *Time-variant space-Doppler (SD) power spectrum density (PSD)*

The SD PSD can be derived as the Fourier transform of the ACF with the respect to Δt, which can be applied to reflect the distribution of power spectrum along the Doppler frequency f_{D},

$$S_{h_{pq}h_{p'q'}}(f_{\mathrm{D}}, t) = \int_{-\infty}^{\infty} r_h(t, \Delta t) \cdot \mathrm{e}^{-\mathrm{j}2\pi f_{\mathrm{D}} \Delta t} \mathrm{d}\Delta t. \tag{41}$$

3 A simulation GBSM for circular tunnel channels

3.1 Description of the wideband simulation circular tunnel channel model

In the theoretical model, it assumes an infinite number of scatters, and cannot be used for simulations in reality. Hence, we need to approximate the continuous distribution of theoretical model with a discrete number of scatterers for the simulation model, which can be used in practical applications. Based on the proposed 3D theoretical tunnel channel model described in Section 2, a sum-of-sinusoids (SoS) based simulation model can be developed by utilizing finite number of effective scatterers. The complex coefficient of the link between the Tx and Rx can be expressed as

$$\begin{aligned}\tilde{h}_{pq}(t, \tau) = (\tilde{h}_{pq,i}^{\mathrm{LoS}}(t) \cdot \delta(i-1) + \sum_{i=1}^{I'_{\mathrm{cluster}}} \tilde{h}_{pq,i}^{\mathrm{SB}}(t)) \cdot \delta(\tau - \tau_i^{\mathrm{SB}}(t)) \\ + \sum_{l=1}^{I''_{\mathrm{cluster}}} \tilde{h}_{pq,l}^{\mathrm{MB}}(t) \cdot \delta(\tau - \tau_l^{\mathrm{MB}}(t)),\end{aligned} \tag{42}$$

where

$$\begin{aligned}\tilde{h}_{pq,1}^{\mathrm{LoS}}(t) = \sqrt{\frac{K_{pq}}{K_{pq}+1}} \mathrm{e}^{-\mathrm{j}\frac{2\pi}{\lambda} \cdot D_{pq}(t)} \\ \times \mathrm{e}^{\mathrm{j}2\pi f_{\mathrm{Rmax}} t \cdot \cos(\tilde{\alpha}_{\mathrm{R}}^{\mathrm{LoS}}(t) - \gamma_{\mathrm{R}}) \cdot \cos \tilde{\beta}_{\mathrm{R}}^{\mathrm{LoS}}(t)},\end{aligned} \tag{43}$$

$$\begin{aligned}\tilde{h}_{pq,i}^{\mathrm{SB}}(t) = \sqrt{\frac{P_i}{K_{pq}+1}} \sum_{n_i=1}^{N_i} \frac{1}{\sqrt{N_i}} \mathrm{e}^{\mathrm{j}(\varphi_{n_i} - \frac{2\pi}{\lambda} \cdot D_{pq}^{in_i}(t))} \\ \times \mathrm{e}^{\mathrm{j}2\pi f_{\mathrm{Rmax}} t \cdot \cos(\tilde{\alpha}_{\mathrm{R}}^{in_i}(t) - \gamma_{\mathrm{R}}) \cdot \cos \tilde{\beta}_{\mathrm{R}}^{in_i}(t)},\end{aligned} \tag{44}$$

$$\begin{aligned}\tilde{h}_{pq,l}^{\mathrm{MB}}(t) = \sqrt{\frac{P_l}{K_{pq}+1}} \sum_{n_l=l}^{N_l} \frac{1}{\sqrt{N_l}} \cdot \mathrm{e}^{\mathrm{j}(\varphi_{n_l} - \frac{2\pi}{\lambda} \cdot D_{pq}^{ln_l}(t))} \\ \times \mathrm{e}^{\mathrm{j}2\pi f_{\mathrm{Rmax}} t \cdot \cos(\tilde{\alpha}_{\mathrm{R}}^{ln_l}(t) - \gamma_{\mathrm{R}}) \cdot \cos \tilde{\beta}_{\mathrm{R}}^{ln_l}(t)}.\end{aligned} \tag{45}$$

By discretizing continuous angular parameters of the theoretical model, the angular parameters of simulation model can be obtained. Here, we use the method of equal volume (MEV) to calculate the discrete angular information.

3.2 MEV for parametrization of the simulation model

To jointly consider the influence of azimuth angles and elevation angles on 3D tunnel channel statistics, the von Mises Fisher (VMF) probability density function (PDF) can be used to characterize the distribution of effective scatterers. The VMF PDF can be expressed as

$$f(\alpha,\beta)=\frac{k_i\cos\beta}{4\pi\sinh k_i}\cdot \mathrm{e}^{k_i[\cos\mu_\beta\cos\beta\cos(\alpha-\mu_\alpha)+\sin\mu_\beta\sin\beta]}, \tag{46}$$

where μ_α and μ_β are the mean values of azimuth angle α and elevation angle β, respectively, and k_i ($k_i\geqslant 0$) is a real-valued parameter of the ith cluster that controls the spread of the distribution relative to the mean direction μ_α and μ_β. Here, k_i values of different clusters are assumed same k so as to simplify the analysis. We define the vector of azimuth angles and elevation angles as $x=\{\alpha,\beta\}$. According to the cumulative distribution function (CDF) of α and β in the theoretical model, we can obtain the discrete vector of angles for the simulation model [18]. For the angular descriptions of cluster, α and β can be replaced by $\{\alpha_{\mathrm{R}}^{in_i}(t),\beta_{\mathrm{R}}^{in_i}(t)\}$ in SB case, and $\{\alpha_{\mathrm{R}}^{ln_l}(t),\beta_{\mathrm{R}}^{ln_l}(t)\}$ in MB case.

3.3 Statistical properties of the simulation model

Based on the theoretical tunnel channel model and its statistical properties, we can derive the corresponding statistical properties of simulation model by using discrete AAoAs and EAoAs.

3.3.1 *Time-variant ST CF*

From (34) and (35), the time-variant ST CF of simulation model can be calculated by

$$\begin{aligned}\tilde{R}_h(t,\Delta x_{\mathrm{T}},\Delta x_{\mathrm{R}},\Delta t)&=\mathrm{E}\left[\tilde{h}_{pq}(t)\cdot\tilde{h}^*_{p'q'}(t-\Delta t)\right]\\&=\tilde{R}_h^{\mathrm{LoS}}(t,\Delta x_{\mathrm{T}},\Delta x_{\mathrm{R}},\Delta t)+\tilde{R}_h^{\mathrm{SB}}(t,\Delta x_{\mathrm{T}},\Delta x_{\mathrm{R}},\Delta t)\\&\quad+\tilde{R}_h^{\mathrm{MB}}(t,\Delta x_{\mathrm{T}},\Delta x_{\mathrm{R}},\Delta t).\end{aligned} \tag{47}$$

For the LoS component, the ST CF can be expressed as

$$\begin{aligned}\tilde{R}_h^{\mathrm{LoS}}(t,\Delta x_{\mathrm{T}},\Delta x_{\mathrm{R}},\Delta t)&=\frac{K_{pq}}{K_{pq}+1}\cdot\mathrm{e}^{\frac{\mathrm{j}2\pi}{\lambda}\cdot(D_{p'q'}(t-\Delta t)-D_{pq}(t))}\\&\quad\times\mathrm{e}^{\mathrm{j}2\pi f_{\mathrm{Rmax}}\cdot\Delta t\cdot\cos(\tilde{\alpha}_{\mathrm{R}}^{\mathrm{LoS}}(t-\Delta t)-\gamma_{\mathrm{R}})\cdot\cos\tilde{\beta}_{\mathrm{R}}^{\mathrm{LoS}}(t-\Delta t)}.\end{aligned} \tag{48}$$

Next, the SB components resulting from the specific cluster is obtained,

$$\begin{aligned}\tilde{R}_h^{\mathrm{SB}}(t,\Delta x_{\mathrm{T}},\Delta x_{\mathrm{R}},\Delta t)&=\frac{P_i}{(K_{pq}+1)N_i}\cdot\sum_{n_i=1}^{N_i}\mathrm{e}^{\frac{\mathrm{j}2\pi}{\lambda}\cdot(D_{p'q'}^{in_i}(t-\Delta t)-D_{pq}^{in_i}(t))}\\&\quad\times\mathrm{e}^{\mathrm{j}2\pi f_{\mathrm{Rmax}}\Delta t\cdot\cos(\tilde{\alpha}_{\mathrm{R}}^{in_i}(t)-\gamma_{\mathrm{R}})\cdot\cos\tilde{\beta}_{\mathrm{R}}^{in_i}(t)}.\end{aligned} \tag{49}$$

Regarding the MB components resulting from twin-cluster, we can get

$$\begin{aligned}\tilde{R}_h^{\mathrm{MB}}(t,\Delta x_{\mathrm{T}},\Delta x_{\mathrm{R}},\Delta t)&=\frac{P_l}{(K_{pq}+1)N_l}\cdot\sum_{n_l=1}^{N_l}\mathrm{e}^{\frac{\mathrm{j}2\pi}{\lambda}\cdot(D_{p'q'}^{ln_l}(t-\Delta t)-D_{pq}^{ln_l}(t))}\\&\quad\times\mathrm{e}^{\mathrm{j}2\pi f_{\mathrm{Rmax}}\Delta t\cos(\tilde{\alpha}_{\mathrm{R}}^{ln_l}(t)-\gamma_{\mathrm{R}})\cos\tilde{\beta}_{\mathrm{R}}^{ln_l}(t)}.\end{aligned} \tag{50}$$

As we should present the spatial components, we rewrite the ST CF as

$$\tilde{\rho}_h(t,\Delta x_{\mathrm{T}},\Delta x_{\mathrm{R}})=\mathrm{E}\left[\tilde{h}_{pq}(t)\cdot\tilde{h}^*_{pq}(t)\right]=\tilde{R}_h(t,\Delta x_{\mathrm{T}},\Delta x_{\mathrm{R}},0). \tag{51}$$

Moreover, by imposing $\Delta x_{\mathrm{R}}=0$ and $\Delta x_{\mathrm{T}}=0$ in (47), the time-variant ACF can be derived as

$$\tilde{r}_h(t,\Delta t)=\mathrm{E}\left[\tilde{h}_{pq}(t)\cdot\tilde{h}^*_{pq}(t-\Delta t)\right]=\tilde{R}_h(t,0,0,\Delta t). \tag{52}$$

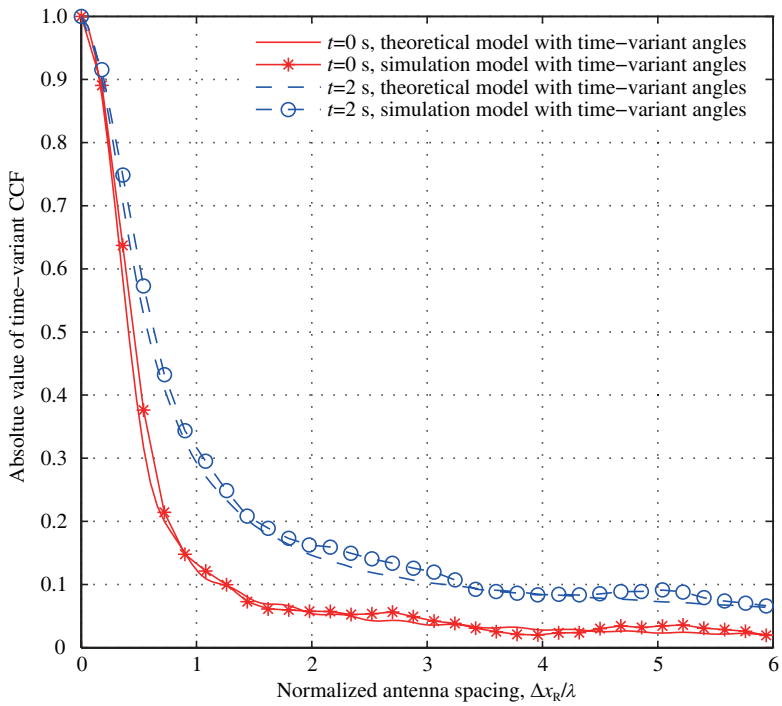

Figure 4 (Color online) Absolute values of the time-variant spatial CCF of the proposed HST tunnel channel model with time-variant angles at different time instants.

3.3.2 *Time-variant SD PSD*

The time-variant SD PSD of the simulation model can be obtained as the Fourier transform of time-variant ACF in terms of Δt, i.e.,

$$\tilde{S}_{\tilde{h}_{pq}\tilde{h}_{p'q'}}(f_{\mathrm{D}},t)=\tilde{S}^{\mathrm{LoS}}_{\tilde{h}_{pq}\tilde{h}_{p'q'}}(f_{\mathrm{D}},t)+\tilde{S}^{\mathrm{SB}}_{\tilde{h}_{pq}\tilde{h}_{p'q'}}(f_{\mathrm{D}},t)+\tilde{S}^{\mathrm{MB}}_{\tilde{h}_{pq}\tilde{h}_{p'q'}}(f_{\mathrm{D}},t). \tag{53}$$

4 Results and analysis

In this section, we investigate the statistical properties of our proposed models in detail. Refer to the channel measurement in tunnel scenarios [23, 26], the following parameters were chosen for simulations: $R=2.65$ m, $v_{\mathrm{R}}=360$ km/h, $f_c=2.4$ GHz, $\gamma_{\mathrm{R}}=0^\circ$, $\phi_{\mathrm{T}}=\phi_{\mathrm{R}}=30^\circ$, $\varphi_{\mathrm{T}}=\varphi_{\mathrm{R}}=0^\circ$, $v_{c\mathrm{T}}=v_{c\mathrm{R}}=0$ km/h, and $K_{pq}=10$ dB [27]. Moreover, a 2×2 MIMO linear antenna array in DAS is considered. The initial coordinates are denoted as $(x_{\mathrm{T}},y_{\mathrm{T}},z_{\mathrm{T}})=(0,\,1.85,\,0)$ at Tx and $(x_{\mathrm{R}},y_{\mathrm{R}},z_{\mathrm{R}})=(300,\,0,\,0)$ at Rx. Here, we assumed the total number of clusters as $I_{\mathrm{cluster}}=8$, and set the initial mean AAoAs, EAoAs, AAoDs, and EAoDs as random numbers following wrap Gaussian distributions.

4.1 Time-variant spatial CCF

By substituting time-variant AAoAs, EAoAs, AAoDs, and EAoDs in (39) and (51), the absolute values of spatial CCF of the proposed model at different time instants are presented in Figure 4. It shows the non-stationarity of the HST tunnel channel model, and even with time-variant AoAs and AoDs, the simulation model can provide a good approximation to the theoretical model at the same time and small antenna spacings.

4.2 Time-variant ACF

By using (40) and (52), Figure 5 shows a comparison between the ACFs of the theoretical model and simulation model at the same time instant, and finally compared with simulation results. In a small

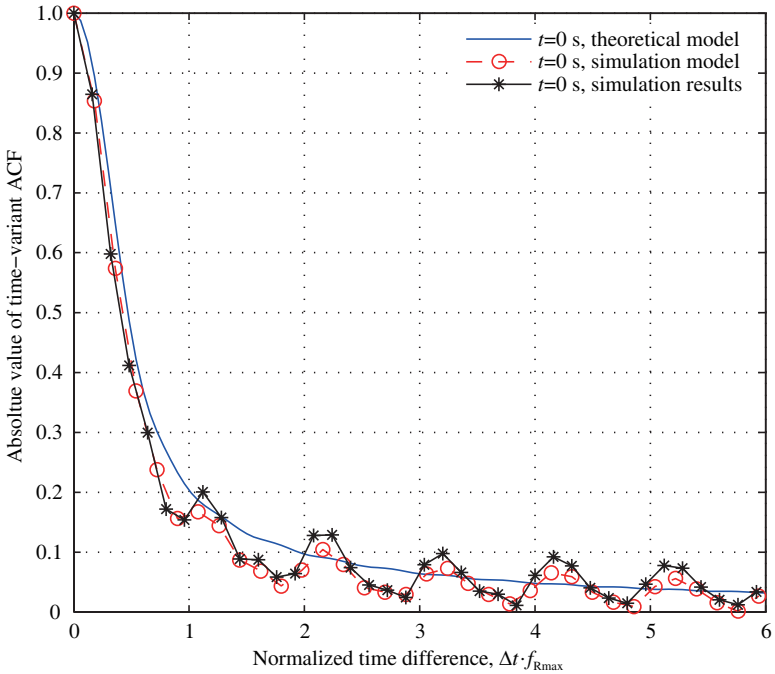

Figure 5 (Color online) Comparison among the time-variant ACFs of the theoretical model, simulation model, and simulation results.

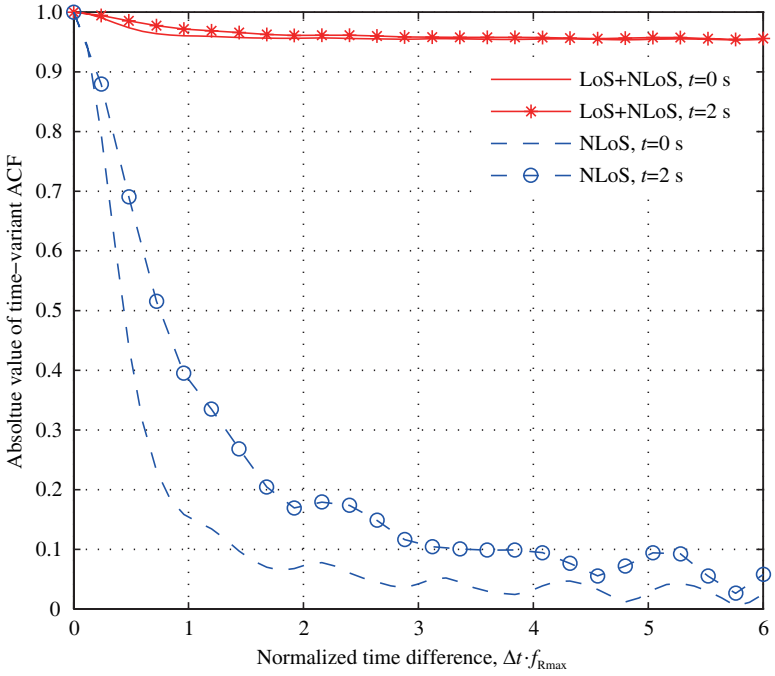

Figure 6 (Color online) Absolute values of the time-variant ACF of the proposed HST tunnel channel model with/without LoS component at different time instants.

time separation, the ACF of simulation model, matches well simulation results, and also provides a good approximation to that of theoretical model.

The absolute values of time-variant ACF of the proposed channel model at different time instants are illustrated in Figure 6. We compare the ACFs of the theoretical model including the LoS component with the non-LoS (NLoS) components. A higher correlation can be observed with LoS component. Moreover, the time-variant properties of the proposed channel model can be seen in Figure 6.

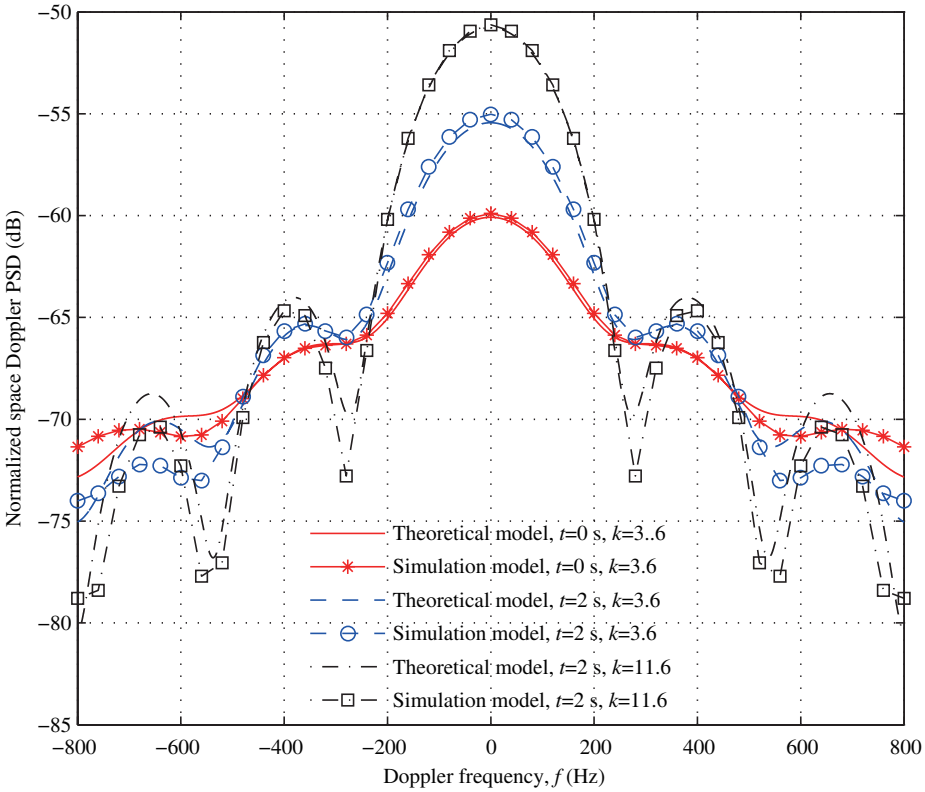

Figure 7 (Color online) Comparison of time-variant SD PSDs of the theoretical and simulation models for different k at different time instants.

Table 2 Comparison of characteristics

Parameter	GBSM	Channel measurement
R (m)	2.65	≈ 2.65
x_{T} (m)	0.01	0.01
y_{T} (m)	1.85	1.79
z_{T} (m)	0	0
x_{R} (m)	150	< 200
y_{R} (m)	0	0
z_{R} (m)	0	0
RMS delay spread (ns)	93.9	93
Coherence bandwidth (MHz)	1.7	≈ 1.6

4.3 Time-variant SD PSD

Figure 7 shows the comparison of time-variant PSDs of the theoretical and simulation models. Due to the non-stationarity of channel, the PSDs exhibit different levels at different time and different von Mises k values. Moreover, the PSDs of the simulation model can fit those of the theoretical model well.

4.4 Comparison with tunnel channel measurements

As shown in Table 2, similar parameters of GBSM are selected according to the channel measurements in [26]. The root mean square (RMS) delay spread and coherence bandwidth of our proposed GBSM tunnel model can match well those in tunnel channel measurements, which demonstrates the accuracy of our proposed tunnel GBSMs.

5 Conclusion

In this paper, a 3D non-stationary theoretical channel model for HST circular tunnel scenarios has been proposed. The corresponding SoS simulation model has also been developed. The statistical properties of both models have been investigated. Numerical analysis has shown that the statistical properties of simulation model approximate closely those of the theoretical model and fit the simulation results well. Moreover, by considering time-variant angles, the statistical properties experience different behaviors at different time instants, demonstrating our proposed models can mimic the non-stationarity of HST tunnel channels. Finally, comparison of our proposed GBSM and channel measurement data has been presented, validating the utility of the proposed model.

Acknowledgements This work was supported by International S&T Cooperation Program of China (Grant No. 2014DFA11640), EU H2020 ITN 5G Wireless Project (Grant No. 641985), EU FP7 QUICK Project (Grant No. PIRSES-GA-2013-612652), EPSRC TOUCAN Project (Grant No. EP/L020009/1), China Scholarship Council (Grant No. 201506450042), and in part by National Natural Science Foundation of China (Grant No. 61210002), Hubei Provincial Science and Technology Department (Grant No. 2016AHB006), and Fundamental Research Funds for the Central Universities (Grant No. 2015XJGH011).

Conflict of interest The authors declare that they have no conflict of interest.

References

1 Wang C X, Wu S B, Bai L, et al. Recent advances and future challenges for massive MIMO channel measurements and models. Sci China Inf Sci, 2016, 59: 021301
2 Ai B, He R, Zhong Z D, et al. Radio wave propagation scene partitioning for high-speed rails. Int J Antenna Propag, 2012, 2012: 1–7
3 Ghazal A, Wang C X, Ai B, et al. A non-stationary wideband MIMO channel model for high-mobility intelligent transportation systems. IEEE Trans Intell Transp Syst, 2015, 16: 885–897
4 Hrovat A, Kandus G, Javornic T. A survey of radio propagation modeling for tunnels. IEEE Commun Surv Tutor, 2014, 16: 658–669
5 Cichon D J, Becker T C, Wiesbeck W. Determination of time-variant radio links in high-speed train tunnels by ray optical modeling. In: Proceedings of Antennas and Propagation Society International Symposium, California, 1995. 508–511
6 Guan K, Ai B, Zhong Z D, et al. The influence of scattering from traffic signs in vehicle-to-x communications. IEEE Trans Veh Tech, 2016, 65: 5835–5849
7 Emslie A G, Lagace R L, Strong P F. Theory of the propagation of UHF radio waves in coal mine tunnels. IEEE Trans Antenna Propag, 1975, 23: 192–205
8 Wang H W, Yu F R, Zhu L, et al. Finite-state markov modeling for wireless channels in tunnel communication-based train control systems. IEEE Trans Intell Transp Syst, 2014, 15: 1083–1090
9 Ge X, Tu S, Han T, et al. Energy efficiency of small cell backhaul networks based on Gauss-Markov mobile models. IET Netw, 2015, 4: 158–167
10 Wang Y H, Zhang Y P, Kouyoumjian R G. Ray-optical prediction of radio-wave propagation characteristics in tunnel environments part 1: theory, part 2: analysis and measurements. IEEE Trans Antenna Propag, 1998, 46: 1328–1345
11 Porrat D. Radio propagation in hallways and streets for UHF communications. Dissertation for Ph.D. Degree. Stanford: Stanford University, 2002
12 Laakmann K D, Steier W H. Waveguides: characteristic modes of hollow rectangular dielectric waveguides. Appl Opt, 1976, 15: 1334–1340
13 Dudley D G. Wireless propagation in circular tunnels. IEEE Trans Antenna Propag, 2005, 53: 435–441
14 Sun Z, Akyildiz I F. Channel modeling and analysis for wireless networks in underground mines and road tunnels. IEEE Trans Commun, 2010, 58: 1758–1768
15 Guan K, Ai B, Fricke A, et al. Excess propagation loss modeling of semi-closed obstacles for intelligent transportation systems. IEEE Trans Intell Transp Syst, 2016, 17: 2171–2181
16 Liu Y, Wang C X, Ghazal A, et al. A multi-mode waveguide tunnel channel model for high-speed train wireless communication systems. In: Proceedings of the 9th European Conference on Antennas and Propagation (EUCAP), Lisbon, 2015. 1–5
17 Avazov N, Patzold M. A novel wideband MIMO car-to-car channel model based on a geometrical semi-circular tunnel scattering model. IEEE Trans Veh Tech, 2016, 65: 1070–1082
18 Yuan Y, Wang C X, Cheng X, et al. 3D geometry-based stochastic models for non-isotropic MIMO vehicle-to-vehicle channels. IEEE Trans Wirel Commun, 2014, 13: 298–309

19 Wang J, Zhu H, Gomes N J. Distributed antenna systems for mobile communications in high speed trains. IEEE J Sel Area Commun, 2012, 30: 675–683
20 Briso-Rodriguez C, Cruz J M, Alonso J I. Measurements and modeling of distributed antenna systems in railway tunnels. IEEE Trans Veh Tech, 2007, 56: 2870–2879
21 Ge X, Qiu Y, Chen J, et al. Wireless fractal cellular networks. IEEE Wirel Commun, 2016, 23: 110–119
22 Guan K, Zhong Z D, Briso-Rodriguez C, et al. Measurements of distributed antenna systems at 2.4 GHz in a realistic subway tunnel environment. IEEE Trans Veh Tech, 2012, 61: 834–837
23 Guan K, Zhong Z, Ai B, et al. Propagation mechanism modelling in the near region of circular tunnels. IET Microw Antenna Propag, 2012, 6: 355–360
24 Wu S, Wang C X, Aggoune H, et al. A non-stationary 3D wideband twin-cluster model for 5G massive MIMO channels. IEEE J Sel Area Commun, 2014, 32: 1207–1218
25 Kyosti P, Meinila J, Hentila L, et al. WINNER D1.1.2 WINNER II channel models ver 1.1, 2007
26 Li J X, Zhou Y P, Zhang J, et al. Radio channel measurements and analysis at 2.4/5 GHz in subway tunnels. J China Commun, 2015, 12: 36–45
27 Cai X, Yin X F, Cheng X, et al. An empirical random-cluster model for subway channels based on passive measurements in UMTS. IEEE Trans Commun, 2016, 64: 3563–3575